

COMPOSITION OF THE INNERMOST CORE COLLAPSE SUPERNOVA EJECTA

C. FRÖHLICH¹, P. HAUSER¹, M. LIEBENDÖRFER², G. MARTÍNEZ-PINEDO³, F.-K. THIELEMANN¹, E. BRAVO⁴, N. T. ZINNER⁵,
W.R. HIX⁶, K. LANGANKE⁷, A. MEZZACAPPA⁶, K. NOMOTO⁸

Draft version October 24, 2018

ABSTRACT

With presently known input physics and computer simulations in 1D, a self-consistent treatment of core collapse supernovae does not yet lead to successful explosions, while 2D models show some promise. Thus, there are strong indications that the delayed neutrino mechanism works combined with a multi-D convection treatment for unstable layers (possibly with the aid of rotation, magnetic fields and/or still existent uncertainties in neutrino opacities). On the other hand there is a need to provide correct nucleosynthesis abundances for the progressing field of galactic evolution and observations of low metallicity stars. The innermost ejecta is directly affected by the explosion mechanism, i.e. most strongly the yields of Fe-group nuclei for which an induced piston or thermal bomb treatment will not provide the correct yields because the effect of neutrino interactions is not included. We apply parameterized variations to the neutrino scattering cross sections in order to mimic in 1D the possible increase of neutrino luminosities caused by uncertainties in proto-neutron star convection. Alternatively, parameterized variations are applied to the neutrino absorption cross sections on nucleons in the “gain region” to mimic the increase in neutrino energy deposition enabled by convective turnover. We find that both measures lead to similar results, causing explosions and a $Y_e > 0.5$ in the innermost ejected layers, due to the combined effect of a short weak interaction time scale and a negligible electron degeneracy, unveiling the proton-neutron mass difference. We include all weak interactions (electron and positron capture, beta-decay, neutrino and antineutrino capture on nuclei, and neutrino and antineutrino capture on nucleons) and present first nucleosynthesis results for these innermost ejected layers to discuss how they improve predictions for Fe-group nuclei. The proton-rich environment results in enhanced abundances of ⁴⁵Sc, ⁴⁹Ti, and ⁶⁴Zn as requested by chemical evolution studies and observations of low metallicity stars as well as appreciable production of nuclei in the mass range up to $A = 80$.

Subject headings: supernovae, nucleosynthesis

1. INTRODUCTION

The problem of core collapse supernova explosions is an old one and the attempts to understand the mechanism have been ongoing for more than 30 years. The idea that a massive star proceeds through all burning stages from H to Si-burning, finally leading to the collapse of the resulting Fe-core to nuclear densities with formation of a neutron star has long been discussed (e.g. Baade & Zwicky 1934; Oppenheimer & Snyder 1939; Arnett & Schramm 1973). Since the 1960s the explosion mechanism has been related to neutrino emission from the hot collapsed core (e.g. Colgate & White 1966; Bethe & Wilson 1985; Bethe 1990) interrupted by a period when it was speculated that the strength of the bounce at nuclear densities could permit shock waves

with sufficient energies to lead to prompt explosions (e.g. Baron et al. 1985, 1987). However, introduction of previously neglected neutrino scattering processes were introduced (e.g. neutrino-electron scattering), which permitted the replacement of lost low energy neutrinos, led to a continuous energy leakage and to the death of the prompt shock within 10 ms after bounce (Bruenn 1989; Myra & Bludman 1989).

Since then, and with the first neutrino detection from a core collapse supernova (SN1987A, see e.g. Koshiba 1992; Burrows 1990), the hope has been that further improvements would lead to successful explosions via energy deposition through neutrino and antineutrino captures on neutrons and protons ($\nu_e + n \rightarrow p + e^-$, $\bar{\nu}_e + p \rightarrow n + e^+$). Two different paths were explored. 1. Convective instabilities, but with still simplified neutrino transport, causing either (a) convective transport in the core and leading to higher neutrino luminosities (e.g. Keil et al. 1996) or (b) higher energy deposition efficiencies in convective regions (Mayle & Wilson 1988; Herant et al. 1994; Janka & Müller 1996; Fryer & Warren 2004). 2. Improved neutrino transport schemes, leading to higher neutrino luminosities via the full solution of the Boltzmann transport equation for neutrino scattering and neutrino reactions (Mezzacappa & Bruenn 1993a,b; Messer et al. 1998).

However, in recent years 1D spherically and 2D rotationally symmetric radiation-hydro calculations have not yet shown successful supernova ex-

¹ Departement für Physik und Astronomie, Universität Basel, CH-4056 Basel, Switzerland

² Canadian Institute for Theoretical Astrophysics, University of Toronto, Toronto ON M5S 3H8, Canada

³ ICREA and Institut d'Estudis Espacials de Catalunya, Universitat Autònoma de Barcelona, E-08193 Barcelona, Spain

⁴ Universitat Politècnica de Catalunya, E-08034 Barcelona, Spain

⁵ Institute of Physics and Astronomy, Aarhus University, Aarhus C, Denmark

⁶ Physics Division, Oak Ridge National Laboratory, Oak Ridge TN 37831-6374, USA

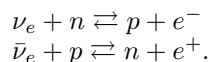
⁷ Gesellschaft für Schwerionenforschung, D-64291 Darmstadt, Germany

⁸ Department of Astronomy, University of Tokyo, Tokyo 113-033, Japan

plosions with the present knowledge of physical processes. (Rampp & Janka 2000; Mezzacappa et al. 2001; Liebendörfer et al. 2001; Liebendörfer et al. 2001; Buras et al. 2003; Janka et al. 2003; Hix et al. 2003; Langanke et al. 2003; Thompson et al. 2003). A very recent simulation of a $11.2 M_{\odot}$ core collapse shows a chance for successful weak explosions in a multi-D treatment with spectral neutrino transport (Janka et al. 2005). This leaves us with two dilemmata. First, the fundamental problem that the supernova mechanism is still not understood. Second, there seems no way to predict the correct supernova nucleosynthesis yields. This is a problem in itself, but is also a limitation for the rapidly expanding field of galactic chemical evolution, which is being energized by the large amount of recent abundance observations from low metallicity stars (e.g. Argast et al. 2002, 2004; Sneden et al. 2003; Cayrel et al. 2004; Honda et al. 2004; Frebel et al. 2005).

Supernova nucleosynthesis predictions have a long tradition (Woosley & Weaver 1986; Thielemann et al. 1990; Woosley & Weaver 1995; Thielemann et al. 1996; Nomoto et al. 1997; Nakamura et al. 2001; Rauscher et al. 2002; Chieffi & Limongi 2002; Chieffi & Limongi 2004; Umeda & Nomoto 2005). But all of these predictions relied on an artificially introduced explosion, either via a piston or a thermal bomb (Aufderheide et al. 1991) introduced into the progenitor star model. The mass cut between the ejecta and the remnant does not emerge from the simulations, but has to be determined from additional conditions. While the usage of artificially introduced explosions is justifiable for the outer stellar layers, provided we know the correct explosion energy to be dumped into the shock front (on the order of 10^{51} erg seen in observations), it clearly is incorrect for the innermost ejected layers which should be directly related to the physical processes causing the explosion. This affects the Fe-group composition, discussed in detail in Thielemann et al. (1996), hereinafter TNH96, and Nakamura et al. (1999), which was also recognized as a clear problem by Chieffi & Limongi (2002) and Umeda & Nomoto (2002). The problem is also linked to the so-called neutrino wind, emitted seconds after the supernova explosion, and considered as a possible source of the r -process to produce the heaviest elements via neutron captures (Takahashi et al. 1994; Woosley et al. 1994; Qian et al. 1997; Thompson et al. 2001; Wanajo et al. 2001; Terasawa et al. 2002; Thompson et al. 2003).

An indispensable quantity to correctly describe nucleosynthesis in the innermost ejecta is the electron fraction $Y_e = \langle Z/A \rangle$ in the layers undergoing explosive Si-burning. This Y_e is set by the weak interactions in the explosively burning layers, i.e. electron and positron captures, beta-decays, and neutrino or antineutrino captures. The dominant reactions in hot photodisintegrated matter, consisting mainly of neutrons and protons, are



In section 4 we will show that these reactions lead to significant changes in Y_e toward equilibrium before the matter is ejected. We will also show that the resulting Y_e in the innermost ejected layers is close to 0.5, in some areas even exceeding 0.5. This has been strongly postu-

lated as a requirement in order not to violate abundance constraints from galactic evolution and solar abundances (TNH96).

The question arises how one could realistically simulate this behavior, given the existing problems with self-consistent explosions. Discussed improvements which could lead to successful supernova explosions are rotation and magnetic fields (e.g. Thompson 2000; Thompson et al. 2004) or uncertainties in neutrino opacities (see e.g. Burrows et al. 2004) or other microphysics properties. They would introduce additional mixing at the neutrino sphere and convective transport or change the neutrino luminosity via improved opacities. This indicates the two options for successful explosion as discussed above: (a) enhanced neutrino luminosities or (b) enhanced deposition efficiencies for neutrino capture in convective layers. These effects can be simulated in two ways: (a) Boosting the neutrino luminosity via a scaling (reduction) of the neutrino scattering cross sections on nucleons while keeping the electron/positron and neutrino/antineutrino capture cross sections on neutrons and protons at their original values. (b) Boosting the energy deposition efficiencies by enhancing the neutrino and antineutrino captures on neutrons and protons. Neither approach represents a self-consistent treatment, but no external energy is required to produce (i) a successful explosion with (ii) a consistently emerging mass cut between neutron star and ejecta. Moreover, our treatment guarantees that Y_e is consistently determined by all weak interaction processes.

2. MATTER IN A NEUTRINO FIELD

Even though it is uncertain how significantly absorptions of the neutrinos emitted from the protoneutron star surface contribute to the revival of the shock, it is necessary to include the neutrinos and their copious interaction with the matter in the vicinity of the protoneutron star. If the explosion is launched such that the mass cut is directly determined by the early dynamics of the explosion, this neutrino heated material will contribute to the deepest layers of the ejecta. If fallback occurs after the initial explosion, contributions by these innermost layers are only possible if strong mixing occurs. In any case, this neutrino heated material will have significantly changed its composition with respect to its original progenitor composition. Hence, we investigate in this section the conditions in ejecta that are subject to large neutrino fluxes.

The energy spectrum of the neutrinos is set in the vicinity of the neutrino spheres at a radius of initially ~ 70 km. Before the launch of the explosion, about two thirds of the emitted neutrinos stem from the infalling matter which is squeezed in the gravitational potential and settles on the surface of the protoneutron star. The rise in the electron energies by the compression leads to more electron neutrino emissions than electron antineutrino emissions. After the launch of the explosion, this contribution will decrease with the accretion rate and the less accretion-sensitive neutrino diffusion flux from the hot protoneutron star will dominate. An energy equipartition among the different neutrino flavors is expected to set in when the accretion luminosities have reduced to a negligible contribution. A more detailed description of this transition, however, requires multi-dimensional

simulations because the evolution of the accretion rate shows quite aspherical features with narrow downflows and broad upflows (Herant et al. 1994; Burrows et al. 1995; Janka & Müller 1996; Buras et al. 2003) that are ignored in spherical symmetry. The emitted electron flavor neutrinos may essentially interact with the material behind the accretion shock out to radii of about 300 km (“essential” meaning electron fraction changes on a time scale of 100 ms). The interactions decrease steeply with increasing radius due to geometric $1/r^2$ dilution of the neutrino field.

In order to illustrate the basic behaviour of shock-heated matter in a neutrino bath, we first consider only the four dominant reactions, electron capture on free protons $e^- + p \rightleftharpoons n + \nu_e$, and positron capture on free neutrons $e^+ + n \rightleftharpoons p + \bar{\nu}_e$, and their inverse reactions. Two independent conditions are required to specify the electron fraction and the entropy of the material, for example weak equilibrium and balance in the energy exchange with neutrinos.

The change of the electron fraction, Y_e , with time, t , is given by Eqs. (C15) and (C20) in Bruenn (1985). The neutrino opacities, χ , and emissivities, j , are linked by the reciprocity relation (detailed balance) described in Eqs. (C7) and (C8) in the above reference. The reciprocity relation involves the temperature, $kT = \beta^{-1}$, the neutrino energy, E , measured in the rest frame of the fluid, and the chemical potentials, μ_n , μ_p , and μ_e , for neutrons, protons, and electrons respectively. We can therefore label contributions from electron, positron, neutrino, and antineutrino capture with EC , PC , NC , and AC respectively, and express the opacities in NC and AC by the neutrino emissivities. After having collected all terms that do not depend on the neutrino energy into a common factor, K , we write the total change in the electron fraction in the following form:

$$\frac{1}{c} \frac{dY_e}{dt} = K \int dE E^2 [h(E+Q)(-EC+NC) + \Theta(E-Q-m_e)h(E-Q)(PC-AC)]. \quad (1)$$

Here, the details of the roughly quadratic energy dependence of the cross sections are hidden in the function

$$h(x) = x^2 \left[1 - \left(\frac{m_e c^2}{x} \right)^2 \right]^{1/2},$$

and a step function $\Theta(x)$ is used to describe the energy threshold in the positron and antineutrino capture reactions. A very similar equation can be used to describe the change of the specific internal energy, e , of the fluid due to neutrino interactions:

$$\frac{1}{c} \frac{de}{dt} = K \int dE E^3 [h(E+Q)(-EC+NC) + \Theta(E-Q-m_e)h(E-Q)(-PC+AC)]. \quad (2)$$

The density in the supernova ejecta is low enough that we can neglect the nucleon degeneracy and nucleon final state blocking described in Eq. (C14) of Bruenn (1985). The contributions to Eqs. (1) and (2) from the individual reactions are given by

$$EC = \frac{1}{1 + e^{\beta(E+Q-\mu_e)}} n_p (1 - f_\nu)$$

$$\begin{aligned} NC &= \frac{e^{\beta(E+Q-\mu_e)}}{1 + e^{\beta(E+Q-\mu_e)}} n_n f_\nu \\ PC &= \frac{1}{1 + e^{\beta(E-Q+\mu_e)}} n_n (1 - f_{\bar{\nu}}) \\ AC &= \frac{e^{\beta(E-Q+\mu_e)}}{1 + e^{\beta(E-Q+\mu_e)}} n_p f_{\bar{\nu}} \end{aligned} \quad (3)$$

where n_n and n_p are the neutron and proton number densities, respectively, and $f(E)$ is the neutrino distribution function in the rest frame of the fluid.

Note that Eqs. (1) and (2) do not presume that the neutrinos are in equilibrium with matter, nor that they assume any particular spectrum. Some of these assumptions, however, lead to useful analytical formulas for the equilibrium electron fraction. Dominance of the neutrino absorption terms has been assumed for the investigation of the r -process in the neutrino wind of a protoneutron star (Qian & Woosley 1996; Thompson et al. 2001); and the cases where emission terms dominate or where the neutrinos are in thermal equilibrium have been analysed in a study of gamma-ray burst fireballs (Beloborodov 2003). The balance between the four reactions in Eq. (3) is determined by the ratio of the neutron and proton number densities and the exponential $\exp(\beta[E \pm Q \mp \mu_e])$. Its energy integral depends on a competition between the neutrino energy, E (in NC and AC populated according to the neutrino distribution functions f), the mass difference between neutrons and protons, Q , and the electron chemical potential, μ_e . Depending on the conditions, any one of these three quantities can assume a dominant influence on the balance in above reactions.

For neutrinos at high energies compared to $|Q - \mu_e|$ the term $\exp(\beta E)$ is large and the neutrino absorption terms, NC and AC in Eq. (3), dominate over neutrino emission. Hence, if the abundance of these high energy neutrinos is large, the equilibrium Y_e is determined by the balance between neutrino and antineutrino absorption and therefore dependent on the unknown neutrino distribution functions. The rate of change of Y_e is given by

$$\frac{dY_e}{dt} \approx \lambda_{\nu_e n} - Y_e (\lambda_{\nu_e n} + \lambda_{\bar{\nu}_e p}). \quad (4)$$

Using Eqs. (64a) and (64b) of Qian & Woosley (1996) for $\lambda_{\nu_e n}$ and $\lambda_{\bar{\nu}_e p}$ and using the fact that neutrino and antineutrino luminosities are similar (upper right panel of Figure 2) it can be shown that $Y_e > 0.5$ is achieved provided that $4(m_n - m_p) > (\varepsilon_{\bar{\nu}} - \varepsilon_\nu)$ (see also Fig. 5 in Qian & Woosley (1996) and the discussion in §3 of Hoffman et al. (1996)).

However, at earlier time, and as long as the eventual ejecta are close to the neutron star, all four reactions in Eq. (3) are active and the neutrino distribution functions are nontrivial functions of the accretion rate, the distance from the neutrino spheres, and the local weak interactions. Changes in the electron fraction are not only determined by the local neutrino fluxes and spectra, but also by the ability of the matter to accept captured electrons or neutrinos at the given conditions. Especially, when the electrons are degenerate the electron chemical potential can dominate the exponential for average neutrino energies. In this case, $\exp(\beta(E+Q-\mu_e))$ in Eq. (3) is small and $\exp(\beta(E-Q+\mu_e))$ becomes large. Hence, neutrino absorption, NC , and positron capture,

PC , are suppressed and the electron fraction decreases because of more prolific electron captures and antineutrino absorptions. Balance is only established when the ratio between proton and neutron number densities has sufficiently decreased to compensate for the suppression of NC and PC introduced by the exponential. This leads to $n_p < n_n$ and an equilibrium electron fraction $Y_e < 0.5$.

Finally, in a plasma with nondegenerate electrons, the electron chemical potential becomes rather small so that the neutron to proton mass difference, Q , may actually dominate the exponentials in the balance equations, making $\exp(\beta(E + Q - \mu_e))$ in Eq. (3) larger and $\exp(\beta(E - Q + \mu_e))$ smaller. Reversing the trend under degenerate conditions, NC and PC are favored and $n_p > n_n$ is assumed in equilibrium. For not too different neutrino and antineutrino fluxes and spectra, equilibrium will establish at $Y_e > 0.5$. According to the analytical investigation in Beloborodov (2003) for the EC and PC reactions, this situation will occur if the electron chemical potential fulfills the condition $\mu_e < Q/2$. The larger binding energy favors protons over neutrons. High electron fractions below $Y_e = 0.5$ have been predicted for supernova explosions (Fuller & Meyer 1995; Thompson 2000). But recent supernova simulations with accurate neutrino transport have even exceeded the estimates, consistently finding values of $Y_e > 0.5$ in the vicinity of the mass cut in explosion settings (Liebendörfer et al. 2001; Buras et al. 2003; Janka et al. 2003; Thompson et al. 2004; Pruet et al. 2005; Fröhlich et al. 2005a).

3. HYDRODYNAMICAL SIMULATIONS

The framework for this investigation are spherically symmetric simulations with implicit general relativistic Boltzmann neutrino transport, see Mezzacappa & Messer (1999) and Liebendörfer et al. (2004) for a detailed description of the code AGILE-BOLTZTRAN. It features a dynamically adaptive grid (Liebendörfer et al. 2002) that concentrates grid points at the developing mass cut. The simulations are performed until the density drops to $\sim 10^6$ g/cm³ in the region of bifurcation between the ejecta and the remnant. At this time, the mass contained in radial mass zones is becoming very small and the run experiences ill-conditioned Jacobian matrices in the Newton-Raphson scheme. The simulations are then continued by an explicit hydrodynamic code until the temperature falls below $T = 2 \times 10^8$ K. This code employs an explicit difference scheme similar to Colgate & White (1966) and a simplified nuclear reaction network as explained in Bravo et al. (1993).

We use two different approaches to enforce explosions in otherwise non-explosive supernova models. We parametrize the neutral current neutrino scattering opacities on free nucleons with a factor ranging from 0.1 to 0.7 and use a finite differencing⁹ that helps to artificially increase the diffusive fluxes in regions of very high matter density. The net result is a faster deleptonization of the protoneutron star such that the neutrino luminosities are boosted in the heating region. For the sake of computational efficiency, this first series of parametrized runs

⁹ According to Eq. (91) in (Mezzacappa & Bruenn 1993a) instead of Eq. (56) in (Liebendörfer et al. 2004), see sections 3.3.2 and 4.1 in the latter reference for details.

TABLE 1
NAME AND PROPERTIES OF THE DISCUSSED RUNS

Run	Parameter	E_{expl} [erg]	m_{cut} [M_{\odot}]	$t_{v>0}$ [s]	t_{end} [s]
A60	60% scatt.	0.24×10^{51}	1.585	0.46	0.64
A40	40% scatt.	0.78×10^{51}	1.511	0.27	0.53
A20	20% scatt.	1.24×10^{51}	1.444	0.20	0.44
B05	factor 5	0.31×10^{51}	1.586	0.38	0.53
B07	factor 7	0.78×10^{51}	1.531	0.26	0.43
B10	factor 10	1.12×10^{51}	1.509	0.24	0.40

NOTE. — The parameter of series A specifies the percentage of neutral current interactions considered in the model. The parameter of series B specifies the reduction of the heating time scale. The time after bounce where we had to stop the runs with neutrino transport is displayed in the last column labelled by t_{end} . The time of the first appearance of positive velocities is given in the column $t_{v>0}$. The mass cut m_{cut} has been determined at the point where the total energy integrated from outside inwards reaches a maximum. The estimate for the explosion energy E_{expl} has been composed from the total energy of the unbound material between the masscut and the shock front at t_{end} (mostly material that was in NSE) and a correction for the total energy of the bound layers ahead of the shock at progenitor composition.

(series A) has been calculated with the lowest possible angular resolution, involving only inwards and outwards propagating neutrinos. However, all of these measures only affect the propagation of neutrinos in the model; the models are still closed and respect energy and lepton number conservation. We expect that series A represents a simplification of the phenomenology of supernovae that would be driven by higher neutrino luminosities than in the standard cases, for example different forms of protoneutron star convection (Wilson & Mayle 1993; Keil et al. 1996; Mezzacappa et al. 1998; Bruenn et al. 2004) or improvements in the uncertain nuclear matter physics.

With progress in computer speed and code parallelization, we were able to perform simulations using standard resolution (6 angular bins, 12 energy groups) for the Boltzmann neutrino transport in the parameter study for series B. Series B also includes the weak magnetism corrections in the neutrino cross sections (Horowitz 2002). Explosions are enforced by multiplying the absorptivities and emissivities (i.e. the reaction rates for forward and backward reactions in $\nu_e + n \rightleftharpoons p + e^-$ and $\bar{\nu}_e + p \rightleftharpoons n + e^+$) in the heating region by equal factors. This reduces the time scale for neutrino heating without changing the important equilibrium Y_e and temperature. We hope to mimic with this approach a potentially increased heating efficiency in the heating region as it is expected in combination with overturn in this convectively unstable domain (Herant et al. 1994; Burrows et al. 1995; Janka & Müller 1996; Mezzacappa et al. 1998; Buras et al. 2003).

All models are based on a progenitor model with a main sequence mass of 20 M_{\odot} (Nomoto & Hashimoto 1988). The parameters in series A and B are chosen such that each series contributes with a barely exploding model, an extremely exploding model (in terms of parameter range, the explosion energy itself seems to saturate around 1.2×10^{51} erg), and a model with average parameter setting. Important properties of the different runs are listed in Table 1.

Figure 1a presents an overview of the shock trajec-

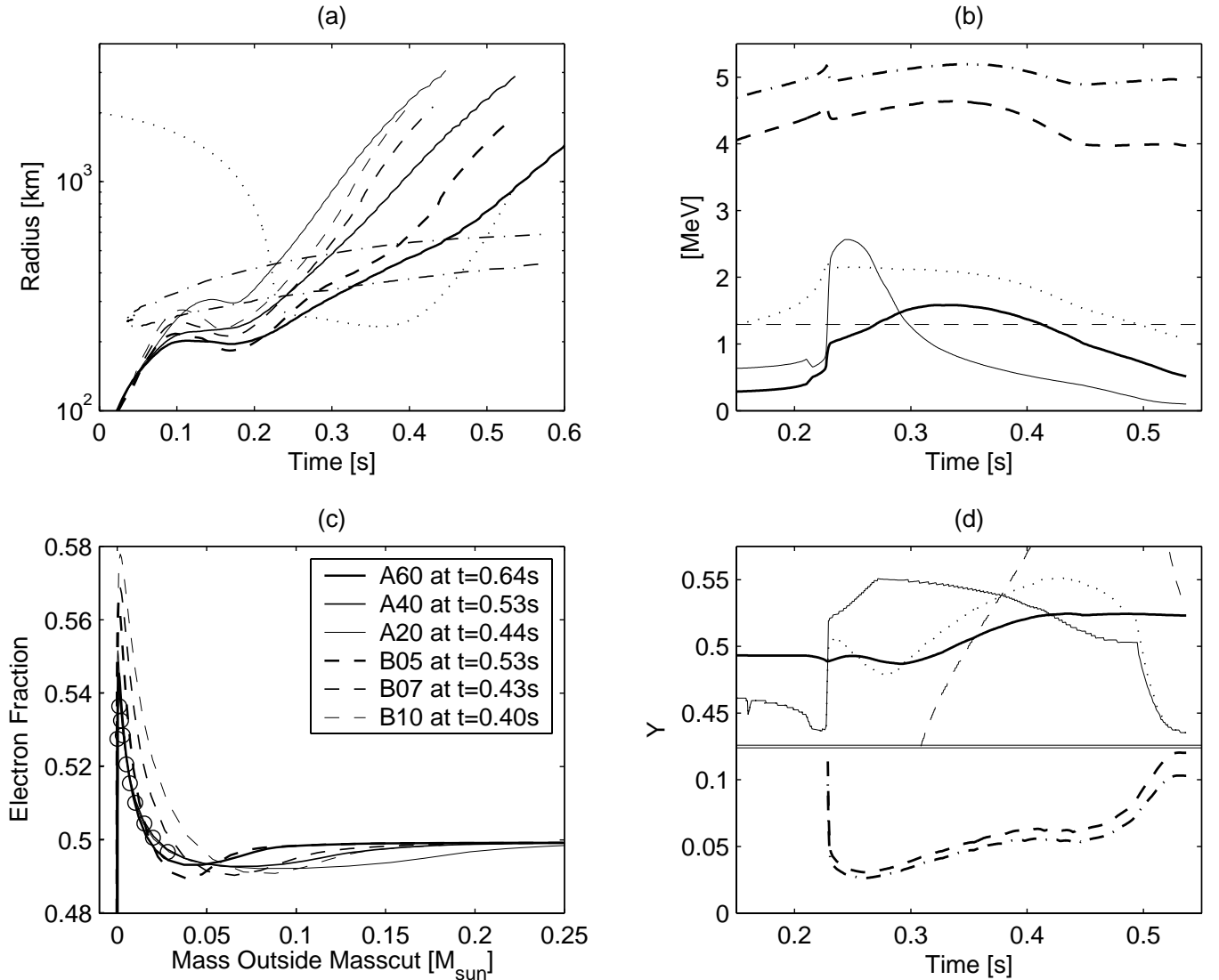


FIG. 1.— (a) Trajectories of the (accretion-) shock as a function of time. Series A (solid lines) explodes because of artificially increased core diffusion luminosities. The neutral current neutrino opacity is used as parameter with 20% of the standard values (thin line), with 40% (medium line width), and with 60% (thick line). Series B (dashed lines) explodes because of artificially accelerated neutrino absorption and emission processes in the heating region. The acceleration factors are 10 (thin line), 7 (medium line width), and 5 (thick line). See also the legend in panel (c) for an identification of the shock trajectories. The dotted line traces the trajectory of a representative fluid element located at $0.005 M_{\odot}$ outside of the estimated mass cut. Its electron fraction and specific energy can change by weak interactions on a time scale represented by the dot-dashed lines (reaction time scale as a function of radius). The lower branch belongs to the infall phase and the upper branch to the ejection.

(b) Energy scales sampled at the representative fluid element as a function of time. Thick lines show the fluid temperature (solid), the neutrino temperature (dashed), and the antineutrino temperature (dot-dashed). Thin lines represent the electron chemical potential (solid), the mass difference between neutron and proton (dashed), and the temperature that would be obtained after infinite exposure to the neutrino field (dotted). The electrons in the representative fluid element are degenerate during collapse and after shock compression. Neutrino heating and expansion during the ejection lifts the electron degeneracy and the neutron to proton mass difference becomes the dominant energy scale.

(c) Electron fraction as function of mass when the runs are stopped (0.4 – 0.6 s after bounce) with (A) reduction of the neutral current scattering opacities (solid lines), or (B) enhancement of the reaction timescales (dashed lines). The open circles represent the final electron fractions of run A40 after the freezeout of charged current interactions.

(d) Abundances sampled at the representative fluid element. Thick lines show the electron fraction (solid), neutrino fraction (dashed), and antineutrino fraction (dot-dashed). Thin lines represent electron fractions that would obtain after infinite exposure to the neutrino field. Only neutrino absorptions have been considered for the solid line and only emissions have been considered for the dashed line. The dotted line includes all charged current reactions. Panel (b) and (d) show that the electron fraction is first kept high by neutrino absorptions, later by neutrino emissions. The electron fraction at freezeout is determined by competition between the neutrino interaction rates and the matter ejection timescale.

ries. Runs from series A are presented with solid lines and runs from series B with dashed lines. The legend in Figure 1c also applies to Figure 1a. In all runs, the accretion front stalls at about 100 ms after bounce at a radius between 180 and 300 km, depending on the parameters. The accretion front is slowly receding in the more optimistic models. Shortly before 200 ms after bounce, the accretion front moves outward again. There may still be some additional delay until the inwards drifting material behind the shock reverses its velocity and starts to accumulate kinetic energy for the ejection. This happens at 199 ms after bounce for the fastest explosion (A20) and at 461 ms after bounce for the slowest run (A60). Bruenn’s suggestion to locate the mass cut where the integrated total energy of all external material assumes a maximum agrees well with the actual bifurcation in the mass trajectories. The mass cuts, m_{cut} , range from $1.444 M_{\odot}$ to $1.585 M_{\odot}$. Realistic 3D calculations where convection (responsible for the corrections applied to the weak rates in both series A and B) turned on in a delayed fashion could delay the explosions and lead to larger mass cuts.

4. CONDITIONS OF MATTER IN THE VICINITY OF THE MASS CUT

In the following, we trace a mass element in the exemplary run A40. We choose a mass element that is $0.005 M_{\odot}$ outside of the mass cut. The trajectory of this mass element is represented in Figure 1a by a dotted line: At first, the element is falling into the gravitational potential. After 200 ms it passes through the accretion shock at about 300 km radius and is instantaneously decelerated. A second phase of drifting around in the heating region follows until about 400 ms after bounce. Finally, the mass element is ejected to larger radii.

Figure 1b illustrates important energy scales along the trajectory. The dashed and dash-dotted thick lines at the top of the graph indicate the neutrino temperature for the electron neutrinos and antineutrinos respectively. They show a rising trend in the first half of the graph. This is because the protoneutron star shrinks and the neutrino spheres become hotter as they shift deeper into the gravitational well. The discontinuity at the crossing of the shock front stems from the Doppler shift when the mass element crosses the velocity jump at the accretion front. The change of the rise into a decline around $t = 350$ ms after bounce is due to the decrease of the accretion rate after the launch of the explosion. Rising neutrino temperatures are resumed at a very small accretion rate after $t = 450$ ms.

With the full neutrino spectrum and abundances from the simulation and with the matter density as input, we calculate the equilibrium matter temperature along the trajectory according to Eq. (2) by requiring $de/dt = 0$. For consistency with the simulation, we have also included the charged current reactions with nuclei according to the simple model described in Bruenn (1985). The dotted line in Figure 1b shows the equilibrium temperature of matter subject to the neutrino luminosities (the neutrinos themselves are not in thermal equilibrium with matter, their temperature is set in the vicinity of the neutrino spheres where the matter temperature is higher). The lower part of Figure 1b shows the matter temperature (thick solid line) and the electron chemical poten-

tial (thin solid line). The electrons are degenerate in the cool infalling matter. The first little blip in the trajectory after $t = 200$ ms is due to the burning of the initial silicon layer to nuclear statistical equilibrium. It causes a slight rise in the temperature and decline in the electron chemical potential. The pronounced step up in both quantities is due to shock compression when the mass element hits the accretion front. During the drift in the heating region, we note a temperature increase towards temperature balance (dotted line) by neutrino heating. The onset of the explosion during this time also leads to an expansion and drop in matter density. Both effects work together to lift the electron degeneracy shortly before 300 ms after bounce (crossing of temperature and electron chemical potential lines). The evolution during the third phase (ejection) is characterised by a density decrease. The weak interaction rates decrease and the temperature declines due to adiabatic expansion. The electrons stay nondegenerate and the electron chemical potential remains smaller than the neutron to proton mass difference (dashed thin line). In contrast to the electron-degenerate conditions found in past supernova simulations that fail to explode, the expanding hot plasma under neutrino irradiation favors electron fractions that exceed 0.5 as discussed in section 2.

The lower part in Figure 1d shows the neutrino and antineutrino abundances with dashed and dash-dotted lines respectively. The variations are due to density changes rather than luminosity variations. The upper part of Figure 1d shows the electron fraction from the simulation (thick solid line) and the equilibrium value determined by Eq. (1) (dotted line). The dash-dotted line in Figure 1a shows the reaction time scale as a function of radius. The upper branch belongs to infall, the lower branch to the ejection. Outside a radius of 600 km the reaction time scale is much larger than the dynamical time scale; during the drift phase of our mass element in the heating region it assumes values around 50 ms. Thus, the low electron fraction during infall is mainly set by the progenitor model. Before the shock front is crossed by the mass trajectory, the equilibrium Y_e is also low because many neutrons are bound in nuclei and not available as targets for antineutrino absorption. After the shock transition, matter is dissociated and higher electron fractions are favored. At first sight, the equilibrium electron fraction appears higher than expected at the given electron degeneracy. The reason are neutrino absorption rates that are by an order of magnitude larger than the neutrino emission rates at these moderate temperatures. The thin solid line shows the high electron fraction equilibrium as it would evolve if only neutrino absorption were considered. The emission reactions alone favor a much lower equilibrium Y_e (thin dashed line) because there are only few positrons to capture under degenerate conditions. With the following rise of the temperature, however, the neutrino emission reactions (e.g. electron capture) gain weight with respect to the absorption reactions and the equilibrium Y_e correspondingly adjusts to lower values in the time window between $t = 235 - 275$ ms. But as the electron degeneracy is lifted with further temperature increase and expansion, and the electron chemical potential dips below half the neutron to proton mass difference, the emission rates start to join the absorption rates in favoring higher electron fractions (steep rise of

the thin dashed line). The equilibrium Y_e increases again. The descent at very late time is, as in the beginning, due to the reappearance of nuclei. The electron fraction in the simulation (thick solid line) can now easily be understood: At each time it evolves towards the equilibrium value for the combined reactions (dotted line) at the pace of the local reaction time scale. It freezes out when the mass element is ejected. Note that for an analytical estimate of the electron fraction in our application one would have to combine the approximations for neutrino absorption rates in Eq. (64) in Qian & Woosley (1996) with the approximation for neutrino emission rates in Eqs. (9-10) in Beloborodov (2003) and to consider the reaction time scale in order to find the correct freeze-out value in the Y_e evolution.

We find that all simulations that lead to an explosion by neutrino heating develop a proton-rich environment around the mass cut with $Y_e > 0.5$. This is illustrated by the electron fraction profiles shown in Figure 1c. The open circles denote the final (i.e. at $T < 2 \times 10^8$ K) electron fraction for the run A40. The mass scale is normalized to the respective mass cut. The different runs from series A show an almost identical electron fraction profile at the mass cut. The competition by the reaction and ejection time scale is not directly influenced by the different explosion parameters, i.e. the enhanced neutrino diffusion at higher densities. The electron fraction profiles of series B, however, respond to the different reaction time scales set by the explosion parameters in the heating region.

The electron fractions around and outside of $m_{\text{cut}} + 0.1 M_{\odot}$ are still close to the progenitor values. Differences in this region stem from the different locations of the mass cuts within the progenitor composition. It is important to note that the investigated region at the mass cut is highly unstable against convection because of a large negative entropy gradient. It is likely that the discrepancies in Y_e are heavily mixed on a dynamical time scale (Kifonidis et al. 2003). We expect, however, that the Y_e remains high in an averaged sense (see also Pruet et al. 2005). Moreover, matter blobs that leave the heating region in an environment of large convective turnover may still show qualitatively similar features in comparison with our spherically symmetric shells, because the high electron fraction in the neutrino field is enabled by the discussed general features of expanding hot matter. We believe that the dependence on the details of our different simulations is small.

5. NUCLEOSYNTHESIS

For the nucleosynthesis results presented here, we consider only the first few zones outside of the mass cut enclosing a few hundredths of a solar mass where values of Y_e higher than 0.5 are achieved. To determine the final electron fraction Y_e in supernova ejecta it is necessary to include neutrino absorption reactions on neutrons and on protons as well as electron and positron captures reactions.

An example of the influence of the individual weak interaction contributions leading to $Y_e > 0.5$ is given in Figure 2 (bottom right) for an exploratory study of one mass zone. Also shown are the neutrino luminosities L_{ν} (top left) and energies $\varepsilon_{\nu} = \langle E_{\nu}^2 \rangle / \langle E_{\nu} \rangle$ (top right). For this exemplary mass zone it can be seen in the upper right

panel of Figure 2 that $(\varepsilon_{\bar{\nu}} - \varepsilon_{\nu})$ is always smaller than $4(m_n - m_p)$. There are several phases that can be identified in Figure 2 and that have been discussed in section 2. At early times ($t < 0.3$ s) matter is degenerate and electron capture dominates. At the same time matter is being heated by neutrino energy deposition and around $t \approx 0.3$ s the degeneracy is lifted (see upper panel of Figure 2). At this time, the ratio between electron captures and positron captures significantly decreases and neutrino absorption reactions start to dominate the change of Y_e and, as discussed before, the average neutrino energies favor $Y_e > 0.5$. As the matter expands the density decreases, reducing the electron chemical potential. This results in positron captures dominating electron captures beginning around $t \approx 0.3$ s. From this time, the combined effect of positron capture and ν_e absorption contributes to the final increase of Y_e .

Figure 3 shows the time evolution for a representative layer of models A40 (scattering cross sections on nucleons reduced by 40%) for the whole computational time. The final decline in the electron fraction Y_e is due to β -decays of the nucleosynthesis products.

The position of the mass cut emerges consistently from the simulation as the region of bifurcation in which the density has dropped below $\sim 10^6$ g/cm³. Based on the temperature-density profiles of all the matter in our hydrodynamical simulation, the detailed nucleosynthesis is calculated in a postprocessing framework for the temperature range $T \geq 2 \times 10^8$ K. The extended nuclear reaction network used consists of 1072 nuclei with $1 \leq Z \leq 50$, see Table 2. Neutral and charged particle reactions are taken from the recent REACLIB compilation (containing experimental rates by Angulo et al. (1999) (NACRE) and theoretical predictions by Rauscher & Thielemann (2000), and are the same as used in Schatz et al. (2001)). For the weak interaction rates (electron/positron captures and beta decays) the rates by Fuller et al. (1982b,a) are used for nuclei with $A \leq 45$ (*sd*-shell). In the mass range $45 < A \leq 65$ (*pf*-shell) the extended tabulation by Langanke & Martínez-Pinedo (2001) is used. In Table 3 a detailed list of nuclei is given for which the above weak rates were utilized. The rates for neutrino and antineutrino captures on nuclei for the whole range of nuclei in the network are taken from a recent calculation (Zinner & Langanke 2004), based on the random phase approximation calculations of Langanke & Kolbe (2001, 2002). A complete list of nuclei for which neutrino and antineutrino capture reaction rates were included is shown in Table 4. Hence, all weak interactions responsible for changes of Y_e are taken into account in the reaction network, namely: neutrino/antineutrino capture on free neutrons and protons, neutrino/antineutrino capture on nuclei, electron/positron capture, and β^-/β^+ decays. Neutrino scattering processes do not contribute to abundance changes and are thus not included in the reaction network used for postprocessing. Nevertheless, neutrino-induced spallation reactions can change the final abundances of some nuclei and we will investigate this in future calculations.

Figure 4 shows the abundances after decay to stability of all nuclei for model A40 integrated over mass zones with $Y_e > 0.5$, including in total $\sim 0.011 M_{\odot}$. For these mass zones, we are only concerned with the Fe-group composition. In Figure 5 integrated abundances after

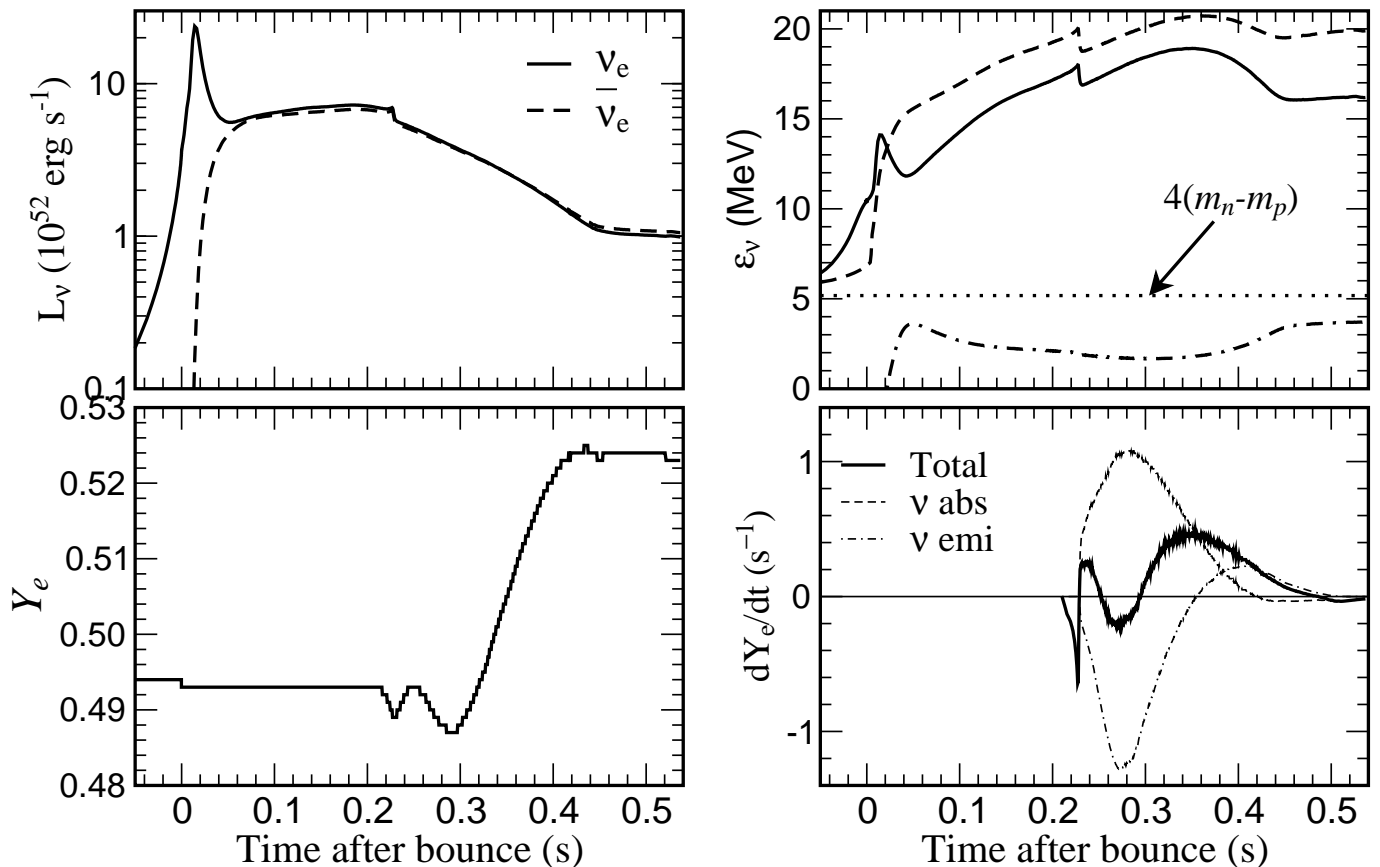


FIG. 2.— Time evolution after core bounce of an ejected layer at $0.005 M_{\odot}$ outside of the mass cut from a $20 M_{\odot}$ supernova progenitor. Top left: Luminosity of neutrinos and antineutrinos felt by a Lagrangian mass zone. Bottom right: Electron fraction Y_e . Top left: Average neutrino energy $\varepsilon_{\nu} = \langle E_{\nu}^2 \rangle / \langle E_{\nu} \rangle$ (thick solid and dashed lines). The difference in average neutrino energy, $(\varepsilon_{\bar{\nu}} - \varepsilon_{\nu})$ (thick dot-dashed line) and four times the mass difference between neutron and protons ($4(m_n - m_p)$) (thin dashed line) are shown in the lower part. Bottom right: Individual weak interaction contributions leading to $Y_e > 0.5$. The individual contributions from neutrino/antineutrino captures and electron/positron captures are a factor ten larger than the total resulting dY_e/dt .

TABLE 2
LIST OF NUCLEI IN REACTION NETWORK

Element	Mass Range	Element	Mass Range	Element	Mass Range
n	1	H	1–3	He	3–6
Li	6–9	Be	7–12	B	8–14
C	9–18	N	11–21	O	13–22
F	15–26	Ne	17–34	Na	17–40
Mg	20–38	Al	21–40	Si	22–42
P	23–48	S	24–50	Cl	26–42
Ar	27–44	K	29–48	Ca	30–50
SC	32–52	Ti	34–54	V	36–56
Cr	38–58	Mn	40–62	Fe	42–64
Co	44–66	Ni	46–68	Cu	48–70
Zn	51–74	Ga	53–86	Ge	55–78
As	57–80	Se	59–84	Br	61–86
Kr	64–92	Rb	66–92	Sr	68–94
Y	70–96	Zr	72–98	Nb	74–100
Mo	77–102	Tc	79–104	Ru	81–108
RH	83–110	Pd	86–114	Ag	88–116
Cd	90–118	In	92–120	Sn	94–126

NOTE. — Nuclear species used in nuclear reaction network for postprocessing. The mass range given indicates for each element the nuclei with the minimum and maximum neutron number.

decay to stability are presented for model B07. In this model, the zones with $Y_e > 0.5$ enclose $\sim 0.0066 M_{\odot}$. The positions of the mass cut and the explosion ener-

gies for both models are given in Table 1. The isotopic abundances (relative to solar values) result from postprocessing based on the hydrodynamical profiles and from employing the full nuclear reaction network including neutrino and antineutrino capture reactions. Note that unlike earlier supernova nucleosynthesis simulations, nuclei beyond $A = 64$ are also produced in appreciable amounts, ranging in fact up to $A = 80$ or even beyond, due to neutrino interactions with matter during the whole period of explosive processing. This is discussed in detail in Fröhlich et al. (2005b). These nuclei are mainly produced in the zones close to the mass cut where the electron fraction depends strongly on neutrino captures. For these mass zones relatively high entropies are attained: $s/k_b \sim 30$ –51. In nucleosynthesis terms this corresponds to complete explosive Si-burning with a strong alpha-rich freeze-out which also leaves a finite proton abundance ($0.0007 M_{\odot}$) due to Y_e being larger than 0.5. The high proton abundance permits the onset of an rp-process which, however, does not proceed too far in A as (due to the high entropies) the densities are too small. The abundances result from the accumulation of matter at the waiting-point nuclei ^{64}Ge , ^{68}Se , ^{72}Kr , ^{76}Sr . After decay to stability they produce the high abundances of ^{64}Zn , ^{68}Zn , ^{72}Ge , and ^{76}Se . A relatively high abundance of ^{78}Kr is also obtained. ^{78}Kr

TABLE 3
NUCLEI FOR WHICH ELECTRON AND POSITRON CAPTURES ARE INCLUDED

Mass Number	Nuclides
1	n, H
21	Mg, Na, Ne, F, O
22	Mg, Na, Ne, F
23	Al, Mg, Na, Ne, F
24	Si, Al, Mg, Na, Ne
25	Si, Al, Mg, Na, Ne
26	Si, Al, Mg, Na
27	P, Si, Al, Mg, Na
28	S, P, Si, Mg, Na
29	S, P, Si, Al, Mg, Na
30	S, P, Si, Al
31	Cl, S, P, Si, Al
32	Ar, Cl, S, P, Si
33	Ar, Cl, S, P, Si
34	Ar, Cl, S, P, Si
35	K, Ar, Cl, S, P
36	Ca, K, Ar, Cl, S
37	Ca, K, Ar, Cl, S
38	Ca, K, Ar, Cl, S
39	Ca, K, Ar, Cl
40	Ti, Sc, Ca, K, Ar, Cl
41	Ti, Sc, Ca, K, Ar, Cl
42	Ti, Sc, Ca, K, Ar
43	Ti, Sc, Ca, K, Ar, Cl
44	V, Ti, Sc, Ca, K, Ar
45	Cr, V, Ti, Sc, Ca, K
46	Cr, V, Ti, Sc, Ca, K
47	Cr, V, Ti, Sc, Ca, K
48	Cr, V, Ti, Sc, Ca, K
49	Fe, Mn, Cr, V, Ti, Sc, Ca, K
50	Mn, Cr, V, Ti, Sc, Ca
51	Mn, Cr, V, Ti, Sc, Ca
52	Fe, Mn, Cr, V, Ti, Sc
53	Co, Fe, Mn, Cr, V, Ti
54	Co, Fe, Mn, Cr, V, Ti
55	Ni, Co, Fe, Mn, Cr, V, Ti
56	Ni, Co, Fe, Mn, Cr, V, Ti, Sc
57	Zn, Cu, Ni, Co, Fe, Mn, Cr, V
58	Cu, Ni, Co, Fe, Mn, Cr, V, Ti
59	Cu, Ni, Co, Fe, Mn, Cr, V
60	Zn, Cu, Ni, Co, Fe, Mn, Cr, V, Ti
61	Zn, Cu, Ni, Co, Fe
62	Ga, Zn, Cu, Ni, Co, Fe
63	Ga, Zn, Cu, Ni, Co, Fe
64	Ge, Ga, Zn, Cu, Ni, Co, Fe
65	Ge, Ga, Zn, Cu, Ni, Co

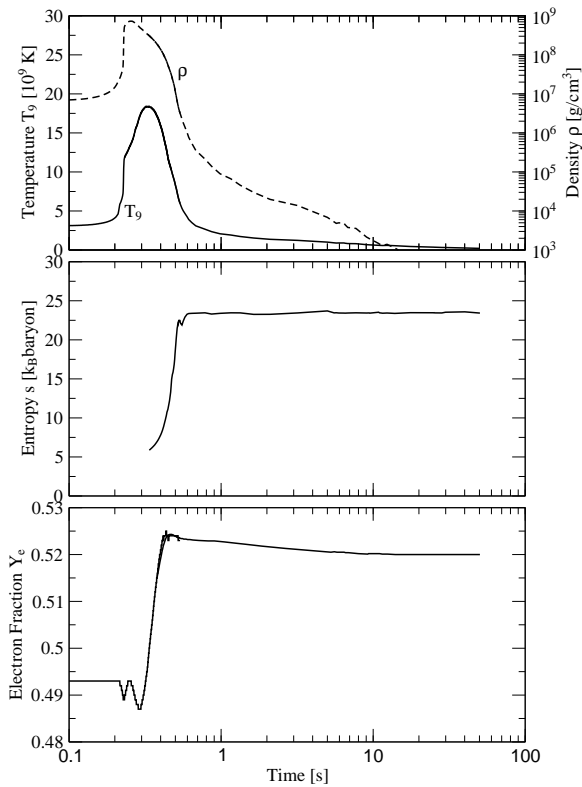


FIG. 3.— Evolution after core bounce for a representative ejected layer at $0.005 M_{\odot}$ outside of the mass cut for model A40. For this layer the time for cooling from $T_9 = 2$ to $T_9 = 0.8$ is about 6 s. Top: Temperature (solid line) and density (dashed line) evolution. Middle: Entropy s per baryon in units of the Boltzmann constant. Bottom: Electron fraction Y_e . The final decline is due to β -decays of the nucleosynthesis products.

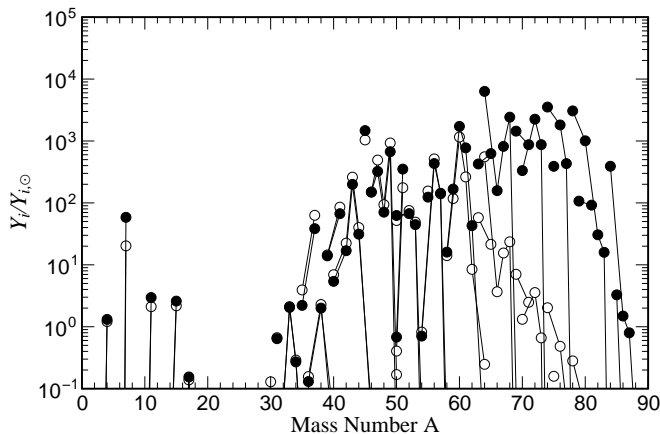


FIG. 4.— Abundances for model A40 relative to solar abundances (Lodders 2003). Two different calculations are shown: with neutrino-induced reactions in the network (filled circles) and without neutrino-induced reactions in the network (open circles).

NOTE. — All nuclei per given mass number for which weak interactions by Fuller et al. (1982b,a) and by Langanke & Martínez-Pinedo (2001) are used in the nuclear network.

is considered to be produced by the p- or γ -process in the ONe layers of the star. Chemical evolution studies (e.g. Timmes et al. 1995) underproduce ^{64}Zn by about a factor 5. A possible site for the production of ^{64}Zn is the modest early-time neutrino-driven wind occurring after core bounce in supernovae (Woosley & Hoffman 1992). Umeda & Nomoto (2005) have found that the $^{64}\text{Zn}/^{56}\text{Fe}$ ratio is enhanced *if* Y_e is close to 0.5 and the explosion energy is as high as $\sim 10^{52}$ erg. Our proton-rich environment constitutes an alternative or complementary production site.

For the intermediate mass elements the main improvement compared to earlier calculations is the higher production of individual nuclei like ^{45}Sc and ^{49}Ti . Scandium

TABLE 4
NUCLEI FOR WHICH NEUTRINO AND ANTI-NEUTRINO CAPTURES ARE INCLUDED

Element	Mass Range (ν capture)	Mass Range ($\bar{\nu}$ capture)
n	1	1
H	1	1
He	6	6
Li	7–9	7–9
Be	8–12	8–12
B	10–14	10–14
C	11–18	11–18
N	13–21	13–21
O	14–22	14–22
F	16–26	16–26
Ne	18–29	17–29
Na	20–32	19–22
Mg	21–35	21–35
Al	22–37	22–37
Si	24–39	23–39
P	26–42	25–42
S	28–42	27–42
Cl	30–42	29–42
Ar	32–44	31–44
K	34–48	33–48
Ca	36–50	35–50
Sc	38–52	37–52
Ti	40–54	39–54
V	42–56	41–56
Cr	44–58	43–58
Mn	45–62	45–62
Fe	48–64	46–64
Co	50–66	49–66
Ni	52–68	51–68
Cu	54–70	53–70
Zn	56–74	55–74
Ga	58–78	57–78
Ge	60–78	59–78
Se	67–84	66–84
Br	69–86	68–86
Kr	71–92	70–92
Rb	73–92	72–92
Sr	77–94	74–92
Y	79–96	78–94
Zr	81–98	80–96
Nb	83–100	82–98
Mo	85–102	84–100
Tc	87–104	86–102
Ru	89–108	88–104
Rh	91–110	90–108
Pd	94–114	92–110
Ag	96–116	95–114
Cd	98–118	97–116
In	100–120	99–119
Sn	—	101–120

NOTE. — Nuclides for which neutrino and anti-neutrino capture reactions are included in the nuclear network. The mass range given indicates for each element the nucleus with the lowest mass number and the nucleus with the highest mass number.

is mainly produced by the β^+ -decays originating from ^{45}Cr and ^{45}V decaying via ^{45}Ti to ^{45}Sc . Different calculations of abundance yields (TNH96, Woosley & Weaver 1995, Chieffi & Limongi 2002) fail to predict the observed abundance of scandium (Gratton & Sneden 1991; Cayrel et al. 2004). Our calculations show that Sc can be consistently produced with iron in the inner regions of the supernova where Y_e is higher than 0.5. The ejected yield of Sc is $10^{-6} M_\odot$ which is a factor of 10 larger than the value obtained for a similar star by TNH96. If we

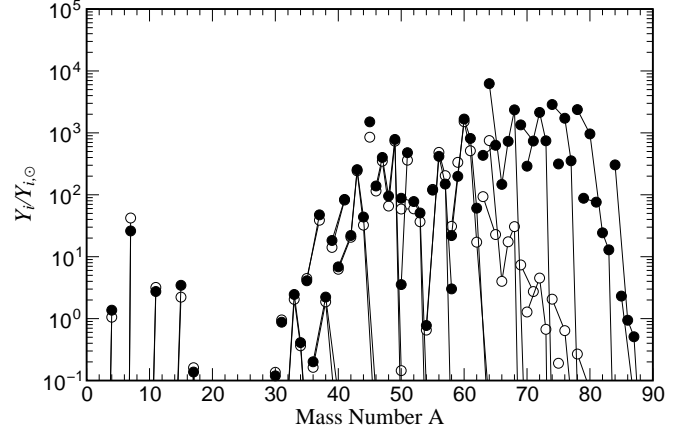


FIG. 5.— Abundances for model B07 relative to solar abundances (Lodders 2003). Two different calculations are shown: with neutrino-induced reactions in the network (filled circles) and without neutrino-induced reactions in the network (open circles).

assume that our total production of Fe is similar to the one obtained in TNH96 our Sc yield will be consistent with observations. ^{49}Ti is underproduced by a factor 5 in the chemical evolution studies of Timmes et al. (1995). The nucleus ^{49}Ti originates from the decay chain of ^{49}Mn which decays via ^{49}Cr and ^{49}V to ^{49}Ti . After decay to stability, the resulting yield of ^{49}Ti is $\sim 5 \times 10^{-6} M_\odot$. We find that the origin of the differences in nucleosynthesis yields is a consequence of an electron fraction above 0.5 which is due to a consistent treatment of all weak interaction processes on free nucleons. The obtained Y_e values are not sensitive to the inclusion of neutrino and antineutrino captures on nuclei.

In the absence of a (yet) complete nucleosynthesis calculation covering the entire region responsible for Fe-group production we combine our abundances with the results of TNH96 (see Figures 6 and 7). The two calculations are combined in such a way that the resulting amount of Fe-group elements is the same as in this earlier work. For the inner zones, where neutrino and antineutrino capture reactions play an important role, the results of the present calculation are used. They constitute about 30% of the total production of Fe-group elements. For the other zones where neutrino/antineutrino captures do not have significant influence on the final Y_e we use the abundance results from TNH96. This procedure allows us to estimate the influence of a consistent treatment of weak interaction processes on the total production of Fe-group elements. To further solidify these results full nucleosynthesis calculations are being performed based on the exploding models.

In a recent work, Pruet et al. (2005) have studied a similar scenario (with a similar philosophy) for the innermost ejected layers, based on a 2D simulation by Janka et al. (2003). While the original 2D simulation did not yield an explosion, omitting the velocity-dependent terms from the neutrino momentum equation resulted in a successful explosion. They find results in agreement with our results. However, they do not report on the production of heavy nuclei with $A > 64$ due to the fact that they utilize the Y_e from the hydrodynamic calculation but do not include neutrino interactions in their network.

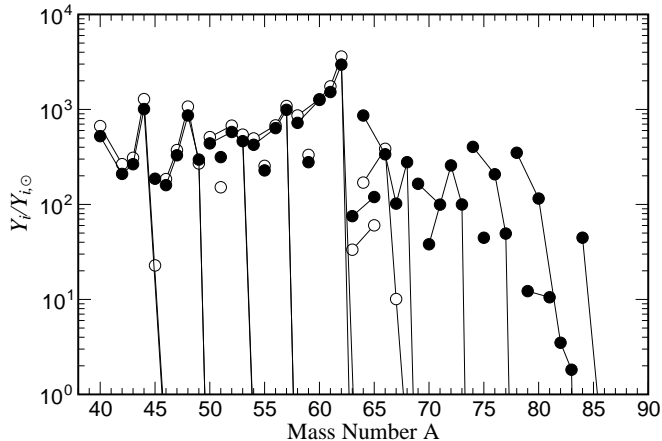


FIG. 6.— Combined abundances of this work (model A40) and TNH96. The open circles are the combined abundances and the filled circles are the original abundances of the above reference. For details see text.

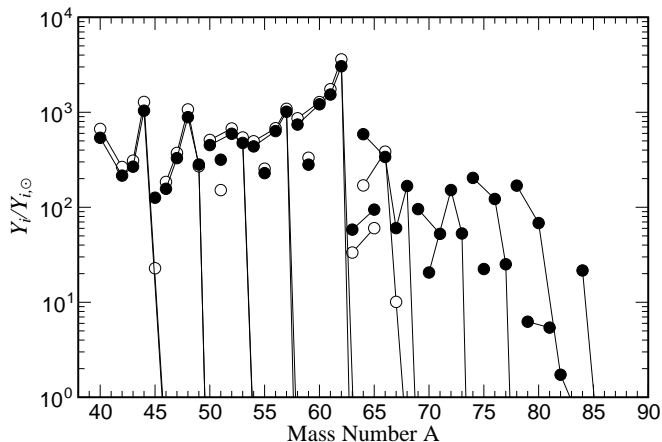


FIG. 7.— Combined abundances of this work (model B07) and TNH96. The open circles are the combined abundances and the filled circles are the original abundances of the above reference. For details see text.

Figure 8 shows elemental abundances of two calculations compared to two sets of observational data. One set of observational data (Gratton & Sneden 1991) originates from a sample of stars with $-2.7 < [\text{Fe}/\text{H}] < -0.8$, relevant for the average type II supernova contribution. The second set of observational data represents a sample of extremely metal-poor stars (Cayrel et al. 2004). The nucleosynthesis results of this work are shown in combination with the results of the earlier calculation as shown in Figure 6 (the results corresponding to Figure 7 are very similar with the exception of Zn and heavier nuclei). For comparison, the theoretical prediction by TNH96 is also shown. We see clearly an improvement for Sc and the heavy elements Cu and Zn.

6. CONCLUSIONS

Presently, self-consistent core collapse supernova simulations in 1D do not lead to successful explosions while 2D models show some promise. Remaining uncertainties in neutrino opacities and/or the expected strong influence of convection (due to hydrodynamic instabilities caused by entropy gradients and/or rotation and magnetic fields) are likely to change this result. They may

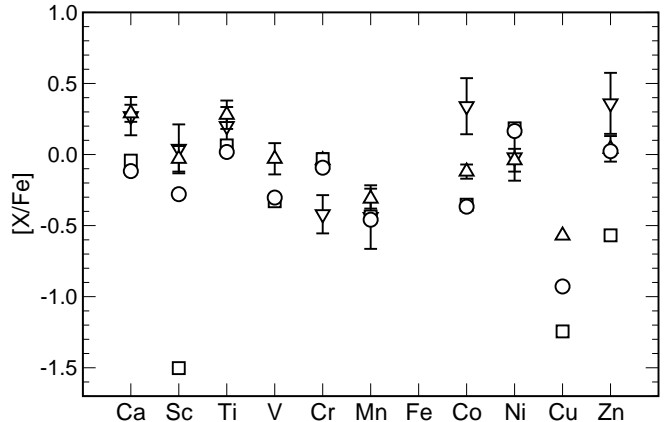


FIG. 8.— Comparison of elemental overabundance in the mass range Ca to Zn for different calculations. The triangles with error bars represent observational data. The triangles facing upwards (Gratton & Sneden 1991) originate from an analysis of stars with $-2.7 < [\text{Fe}/\text{H}] < -0.8$. The triangles facing downwards (Cayrel et al. 2004) is data for a sample of extremely metal poor stars ($-4.1 < [\text{Fe}/\text{H}] < -2.7$). The circles are abundances of this work combined with the work of TNH96 to obtain the same amount of Fe-group elements. The squares show the pure abundances of the previous reference.

lead either to higher neutrino luminosities or higher efficiencies of neutrino energy deposition via neutrino and antineutrino captures on nucleons. In order to examine the accompanied nucleosynthesis in 1D calculations of successful explosions, we performed simulations with variations in neutrino scattering cross sections on nucleons and/or neutrino and antineutrino captures on neutrons and protons. In both cases successful explosions emerge with an interesting evolution of the Y_e gradient in the innermost ejecta, which were followed up by a postprocessing for nucleosynthesis purposes.

The detailed nucleosynthesis calculations with a consistent treatment of all weak interactions show an electron fraction $Y_e > 0.5$, i.e. a slightly proton-rich environment with relatively high entropies of up to $\sim 50 k_B$ per nucleon. This causes complete Si-burning with an alpha-rich (and proton-rich) freeze-out. About $0.0007 M_\odot$ of hydrogen remain in the innermost ejecta and do not stem from mixing this matter in from the hydrogen envelope. Such a proton-rich environment at relatively high entropies permits to produce also nuclei beyond $A=64$, up to $A=80$, with a major contribution to ^{64}Zn . The rp-like process does not extend to masses beyond $A=80-100$ as the high entropies imply too small densities for a path at very small proton separation energies.

In addition, we find improvements within the Fe-group. The strong overabundances of $^{58,62}\text{Ni}$ found in previous (too neutron-rich) environments are reduced. ^{45}Sc and ^{49}Ti are enhanced to permit predictions closer to solar proportions. Especially the emergence of ^{45}Sc seems to be a solution to the previously not understood abundance of this only stable isotope of Sc. This discussion is also of interest with respect to ^{44}Ti , made in the alpha-rich freeze-out in the inner explosive ejecta. ^{44}Ti is sensitive to Y_e and reduced in the mass range where ^{45}Sc is high. This will influence the overall predictions of ^{44}Ti .

Values of $Y_e > 0.5$ are due to the neutrino interactions with matter under electron non-degenerate conditions in

a convectively unstable domain and thus related to the explosion mechanism. The effect of neutrinos decreases with $1/r^2$ and about 50-60% of the Fe-group ejecta (the outer part of explosive, complete Si-burning) is determined by values of Y_e equal to or close to the initial values inherited from stellar evolution. In this first study we have tried to give an estimate for the overall Fe-group composition based on such a superposition of the present results for the innermost ejecta with those of TNH96. Future investigations will require to perform full nucleosynthesis calculation for complete stars based on these exploding models. They will also require a sensitivity test of the nucleosynthesis results to the scaling factors for neutrino-induced reactions discussed in Figure 1 and in combination with the position of the mass cut and the explosion energy. This should be considered in order to reproduce results for supernovae where detailed observational information in abundances, gamma-ray emitters and explosion energies is available.

This work is partly supported by the Swiss SNF grant 200020-105328 and by the Spanish MCyT and European Union ERDF under contracts AYA2002-04094-C03-02 and AYA2003-06128. The neutrino transport calculations have been performed on the CITA Itanium I. The work has been partly supported by the United States National Science Foundation under contract PHY-0244783, by the United States Department of Energy, through the Scientific Discovery through Advanced Computing Program. Oak Ridge National Laboratory is managed by UT-Battelle, LLC, for the U.S. Department of Energy under contract DE-AC05-00OR22725. A.M. is supported at the Oak Ridge National Laboratory, which is managed by UT-Battelle, LLC for the DOE under contract DE-AC05-00OR22725. He is also supported in part by a DOE ONP Scientific Discovery through Advanced Computing Program grant.

REFERENCES

- Angulo, C., Arnould, M., Rayet, M., Descouvemont, P., Baye, D., Leclercq-Willain, C., Coc, A., Barhoumi, S., Aguer, P., Rolfs, C., Kunz, R., Hammer, J. W., Mayer, A., Paradellis, T., Kossionides, S., Chronidou, C., Spyrou, K., Degl'Innocenti, S., Fiorentini, G., Ricci, B., Zavatarelli, S., Providencia, C., Wolters, H., Soares, J., Gram, C., Rahighi, J., Shotter, A., & Rächti, M. L. 1999, *Nucl. Phys. A*, 656, 3
- Argast, D., Samland, M., Thielemann, F.-K., & Gerhard, O. E. 2002, *A&A*, 388, 842
- Argast, D., Samland, M., Thielemann, F.-K., & Qian, Y.-Z. 2004, *A&A*, 416, 997
- Arnett, W. D. & Schramm, D. N. 1973, *ApJ*, 184, L47
- Aufderheide, M. B., Baron, E., & Thielemann, F.-K. 1991, *ApJ*, 370, 630
- Baade, W. & Zwicky, F. 1934, *Proceedings of the National Academy of Science*, 20, 259
- Baron, E., Bethe, H. A., Brown, G. E., Cooperstein, J., & Kahana, S. 1987, *Phys. Rev. Lett.*, 59, 736
- Baron, E., Cooperstein, J., & Kahana, S. 1985, *Phys. Rev. Lett.*, 55, 126
- Beloborodov, A. M. 2003, *ApJ*, 588, 931
- Bethe, H. A. 1990, *Rev. Mod. Phys.*, 62, 801
- Bethe, H. A. & Wilson, J. R. 1985, *ApJ*, 295, 14
- Bravo, E., Dominguez, I., Isern, J., Canal, R., Hoefflich, P., & Labay, J. 1993, *A&A*, 269, 187
- Bruenn, S. W. 1985, *ApJS*, 58, 771
- Bruenn, S. W. 1989, *ApJ*, 340, 955
- Bruenn, S. W., Raley, E. A., & Mezzacappa, A. 2004, *astro-ph/0404099*
- Buras, R., Rampp, M., Janka, H.-T., & Kifonidis, K. 2003, *Phys. Rev. Lett.*, 90, 241101
- Burrows, A. 1990, *Ann. Rev. Nucl. Part. Sci.*, 40, 181
- Burrows, A., Hayes, J., & Fryxell, B. A. 1995, *ApJ*, 450, 830
- Burrows, A., Reddy, S., & Thompson, T. A. 2004, *Nucl. Phys. A*, in press
- Cayrel, R., Depagne, E., Spite, M., Hill, V., Spite, F., François, P., Plez, B., Beers, T., Primas, F., Andersen, J., Barbuy, B., Bonifacio, P., Molaro, P., & Nordström, B. 2004, *A&A*, 416, 1117
- Chieffi, A. & Limongi, M. 2002, *ApJ*, 577, 281
- Chieffi, A. & Limongi, M. 2004, *ApJ*, 608, 405
- Colgate, S. A. & White, R. H. 1966, *ApJ*, 143, 626
- Frebel, A., Aoki, W., Christlieb, N., Ando, H., Asplund, M., Barklem, P. S., Beers, T. C., Eriksson, K., Fechner, C., Fujimoto, M. Y., Honda, S., Kajino, T., Minezaki, T., Nomoto, K., Norris, J. E., Ryan, S. G., Takada-Hidai, M., Tsangarides, S., & Yoshii, Y. 2005, *Nature*, 434, 871
- Fröhlich, C., Hauser, P., Liebendörfer, M., Martínez-Pinedo, G., Bravo, E., Hix, W. R., Zinner, N. T., & Thielemann, F.-K. 2005a, *Nucl. Phys. A*, 758, 27, (*astro-ph/0408067*)
- Fröhlich, C., Martínez-Pinedo, G., Liebendörfer, M., Thielemann, F.-K., Bravo, E., Hix, W. R., Langanke, K., & Zinner, N. T. 2005b, PRL submitted.
- Fryer, C. L. & Warren, M. S. 2004, *ApJ*, 601, 391
- Fuller, G. M., Fowler, W. A., & Newman, M. J. 1982a, *ApJ*, 252, 715
- 1982b, *ApJS*, 48, 279
- Fuller, G. M. & Meyer, B. S. 1995, *ApJ*, 453, 792
- Gratton, R. G. & Sneden, C. 1991, *A&A*, 241, 501
- Herant, M., Benz, W., Hix, W. R., Fryer, C. L., & Colgate, S. A. 1994, *ApJ*, 435, 339
- Hix, W. R., Messer, O. E. B., Mezzacappa, A., Liebendörfer, M., Sampaio, J., Langanke, K., Dean, D. J., & Martínez-Pinedo, G. 2003, *Phys. Rev. Lett.*, 91, 201102
- Hoffman, R. D., Woosley, S. E., Fuller, G. M., & Meyer, B. S. 1996, *ApJ*, 460, 478
- Honda, S., Aoki, W., Ando, H., Izumiura, H., Kajino, T., Kambe, E., Kawanomoto, S., Noguchi, K., Okita, K., Sadakane, K., Sato, B., Takada-Hidai, M., Takeda, Y., Watanabe, E., Beers, T. C., Norris, J. E., & Ryan, S. G. 2004, *ApJS*, 152, 113
- Horowitz, C. J. 2002, *Phys. Rev. D*, 65, 083005
- Janka, H.-T., Buras, R., Kitaura Joyanes, F., Marek, A., Rampp, M., & Scheck, L. 2005, *Nucl. Phys. A*, 758, 19c
- Janka, H.-T., Buras, R., & Rampp, M. 2003, *Nucl. Phys. A*, 718, 269
- Janka, H.-T. & Müller, E. 1996, *A&A*, 306, 167
- Keil, W., Janka, H.-T., & Müller, E. 1996, *ApJ*, 473, L111+
- Kifonidis, K., Plewa, T., Janka, H.-T., & Müller, E. 2003, *A&A*, 408, 621
- Koshiha, M. 1992, *Phys. Rep.*, 220, 229
- Langanke, K. & Kolbe, E. 2001, *At. Data Nucl. Data Tables*, 79, 293
- 2002, *At. Data Nucl. Data Tables*, 82, 191
- Langanke, K. & Martínez-Pinedo, G. 2001, *At. Data Nucl. Data Tables*, 79, 1
- Langanke, K., Martínez-Pinedo, G., Messer, O. E. B., Sampaio, J. M., Dean, D. J., Hix, W. R., Mezzacappa, A., Liebendörfer, M., Janka, H.-T., & Rampp, M. 2003, *Phys. Rev. Lett.*, 90, 241102
- Liebendörfer, M., Messer, O. E. B., Mezzacappa, A., Bruenn, S. W., Cardall, C. Y., & Thielemann, F.-K. 2004, *ApJS*, 150, 263
- Liebendörfer, M., Mezzacappa, A., & Thielemann, F.-K. 2001, *Phys. Rev. D*, 63, 104003
- Liebendörfer, M., Rosswog, S., & Thielemann, F.-K. 2002, *ApJS*, 141, 229
- Liebendörfer, M., Mezzacappa, A., Thielemann, F.-K., Messer, O. E. B., Hix, W. R., & Bruenn, S. W. 2001, *Phys. Rev. D*, 63, 103004
- Lodders, K. 2003, *ApJ*, 591, 1220
- Mayle, R. & Wilson, J. R. 1988, *ApJ*, 334, 909
- Messer, O. E. B., Mezzacappa, A., Bruenn, S. W., & Guidry, M. W. 1998, *ApJ*, 507, 353

- Mezzacappa, A. & Bruenn, S. W. 1993a, *ApJ*, 405, 637
 —. 1993b, *ApJ*, 410, 740
- Mezzacappa, A., Calder, A. C., Bruenn, S. W., Blondin, J. M., Guidry, M. W., Strayer, M. R., & Umar, A. S. 1998, *ApJ*, 495, 911
- Mezzacappa, A., Liebendörfer, M., Messer, O. E. B., Hix, W. R., Thielemann, F.-K., & Bruenn, S. W. 2001, *Phys. Rev. Lett.*, 86, 1935
- Mezzacappa, A. & Messer, O. E. B. 1999, *Journal of Computational and Applied Mathematics*, 109, 281
- Myra, E. S. & Bludman, S. A. 1989, *ApJ*, 340, 384
- Nakamura, T., Umeda, H., Iwamoto, K., Nomoto, K., Hashimoto, M., Hix, W. R., & Thielemann, F. 2001, *ApJ*, 555, 880
- Nakamura, T., Umeda, H., Nomoto, K., Thielemann, F., & Burrows, A. 1999, *ApJ*, 517, 193
- Nomoto, K. & Hashimoto, M. 1988, *Phys. Rep.*, 163, 13
- Nomoto, K., Hashimoto, M., Tsujimoto, T., Thielemann, F.-K., Kishimoto, N., Kubo, Y., & Nakasato, N. 1997, *Nucl. Phys. A*, 616, 79
- Oppenheimer, J. R. & Snyder, H. 1939, *Phys. Rev.*, 56, 455
- Pruet, J., Woosley, S. E., Buras, R., Janka, H.-T., & Hoffman, R. D. 2005, *ApJ*, 623, 325
- Qian, Y. Z., Haxton, W. C., Langanke, K., & Vogel, P. 1997, *Phys. Rev. C*, 55, 1532
- Qian, Y.-Z. & Woosley, S. E. 1996, *ApJ*, 471, 331
- Rampp, M. & Janka, H.-T. 2000, *ApJ*, 539, L33
- Rauscher, T., Heger, A., Hoffman, R. D., & Woosley, S. E. 2002, *ApJ*, 576, 323
- Rauscher, T. & Thielemann, F.-K. 2000, *At. Data Nucl. Data Tables*, 75, 1
- Schatz, H., Aprahamian, A., Barnard, V., Bildsten, L., Cumming, A., Ouellette, M., Rauscher, T., Thielemann, F.-K., & Wiescher, M. 2001, *Phys. Rev. Lett.*, 86, 3471
- Snedden, C., Cowan, J. J., Lawler, J. E., Ivans, I. I., Burles, S., Beers, T. C., Primas, F., Hill, V., Truran, J. W., Fuller, G. M., Pfeiffer, B., & Kratz, K. 2003, *ApJ*, 591, 936
- Takahashi, K., Witt, J., & Janka, H.-T. 1994, *A&A*, 286, 857
- Terasawa, M., Sumiyoshi, K., Yamada, S., Suzuki, H., & Kajino, T. 2002, *ApJ*, 578, L137
- Thielemann, F.-K., Hashimoto, M., & Nomoto, K. 1990, *ApJ*, 349, 222
- Thielemann, F.-K., Nomoto, K., & Hashimoto, M. 1996, *ApJ*, 460, 408, (TNH96)
- Thompson, C. 2000, *ApJ*, 534, 915
- Thompson, T. A., Burrows, A., & Meyer, B. S. 2001, *ApJ*, 562, 887
- Thompson, T. A., Burrows, A., & Pinto, P. A. 2003, *ApJ*, 592, 434
- Thompson, T. A., Quataert, E., & Burrows, A. 2004, astro-ph/0403224
- Timmes, F. X., Woosley, S. E., & Weaver, T. A. 1995, *ApJS*, 98, 617
- Umeda, H. & Nomoto, K. 2002, *ApJ*, 565, 385
- . 2005, *ApJ*, 619, 427
- Wanajo, S., Kajino, T., Mathews, G. J., & Otsuki, K. 2001, *ApJ*, 554, 578
- Wilson, J. R. & Mayle, R. W. 1993, *Phys. Rep.*, 227, 97
- Woosley, S. E. & Hoffman, R. D. 1992, *ApJ*, 395, 202
- Woosley, S. E. & Weaver, T. A. 1986, *ARA&A*, 24, 205
- Woosley, S. E. & Weaver, T. A. 1995, *ApJS*, 101, 181
- Woosley, S. E., Wilson, J. R., Mathews, G. J., Hoffman, R. D., & Meyer, B. S. 1994, *ApJ*, 433, 229
- Zinner, T. N. & Langanke, K. 2004, private communication